Sustainable Energy & Fuels

ROYAL SOCIETY OF CHEMISTRY

PAPER

View Article Online
View Journal | View Issue

Cite this: *Sustainable Energy Fuels*, 2025, **9**, 2813

Received 27th January 2025
Accepted 16th April 2025

DOI: 10.1039/d5se00130g

rsc.li/sustainable-energy

Vacancy enhanced Li, Na, and K clustering on graphene†

Jonathon Cottom,[ac] Qiong Cai[b] and Emilia Olsson*[ac]

The formation of metallic dendrites during battery cycling is a persistent challenge for alkali metal-ion batteries, reducing cycle life and posing safety risks. Although surface defects are often implicated in inhomogeneous metal nucleation, the atomic-scale mechanisms by which they promote metal clustering and subsequent dendrite formation remain poorly understood. Here, we use first-principles calculations to investigate how carbon monovacancies (V_C) influence the clustering behaviour of alkali metals (Li, Na, and K) on graphene – a common basal-plane motif in graphite, hard carbons, and graphene-based anodes. Clusters of Li, Na, and K of varying size (M_n for $n \in \{1–12\}$) are characterised on pristine and defective graphene to understand their stability. On pristine graphene, cluster formation is hindered for Li due to the instability of small clusters ($n \leq 3$) and significant Li–Li repulsion, and suppressed for K due to weak K–K binding and its larger ionic radius. In contrast, Na exhibits spontaneous clustering, suggesting a higher propensity for dendrite formation even in the absence of defects. The introduction of a V_C dramatically alters these trends: it stabilises small ($n \leq 3$) clusters across all three metals by enhancing binding strength with the surface and modifying charge localisation. For Li, the vacancy overcomes the barrier to early-stage nucleation; for Na, it promotes growth at even lower metal loadings; and for K, clustering becomes locally favoured albeit only for the smallest cluster sizes ($n \leq 3$). These results clarify the defect-facilitated pathways to metal clustering, offering atomistic insight that can inform the development of more dendrite-resistant carbon architectures.

1. Introduction

As human society seeks sustainable energy solutions, the development of efficient storage technologies has become pivotal in reducing the dependency on fossil fuels. Lithium-ion batteries (LIBs) have long been central to this effort due to their high energy density and efficiency across a wide range of applications.[1–3] However, with growing demand straining global lithium (Li) resources, exploring viable alternatives and complementary technologies is essential.[4–9] Sodium (Na) and potassium (K), situated alongside lithium in the periodic table, offer promising pathways toward cost-effective, large-scale energy storage systems that can alleviate pressure on lithium supplies. Sodium-ion (NIBs) and potassium-ion batteries (KIBs) are emerging as feasible options for applications where weight constraints are less critical, enabling LIBs to be prioritized for weight-sensitive applications.[10–13]

Alkali metal-ion batteries (MIBs), including lithium, sodium, and potassium, share common design elements: a layered cathode, a liquid electrolyte, and (typically) a carbon-based anode. A wide range of carbonaceous anode materials—graphite, graphene, hard and soft carbons, and carbon nanotubes—have been implemented across these systems with varying degrees of success, each offering distinct surface morphologies, porosities, and electronic properties.[14–17] In parallel, carbon materials are increasingly being explored as interlayer components in solid-state battery architectures, where they facilitate alkali metal plating and stripping while improving mechanical contact with solid electrolytes.[12,18,19] Despite their morphological diversity, these materials exhibit sp^2-hybridized frameworks of six-membered carbon rings, forming planar or quasi-planar basal surfaces reminiscent of graphene.[16,18,20–24] This structural commonality establishes graphene both as a candidate anode material and as a prototypical model for investigating alkali metal interactions on carbon surfaces.[25–31]

The electrochemical performance of MIBs remains constrained by persistent challenges related to stability and cycle life, particularly under fast-charging conditions.[8,12,32,33] A critical bottleneck is the uncontrolled nucleation of metal at the anode, which initiates dendritic growth and irreversible plating.[34–38] These filamentary structures, resulting from inhomogeneous

---

[a] Advanced Research Center for Nanolithography, Science Park 106, Amsterdam, 1098 XG, The Netherlands

[b] School of Chemistry and Chemical Engineering, University of Surrey, Guildford, GU2 7XH, UK

[c] Institute of Theoretical Physics, Institute of Physics, University of Amsterdam, Science Park 904, Amsterdam, 1098 XH, The Netherlands. E-mail: k.i.e.olsson@uva.nl

† Electronic supplementary information (ESI) available. See DOI: https://doi.org/10.1039/d5se00130g

deposition at the anode–electrolyte interface, pose severe safety risks through potential short-circuiting.[16,19,39,40] Although solid-state batteries (ASSBs) were conceived to suppress dendrite formation by replacing liquid electrolytes with mechanically rigid solids, Li and Na dendrites continue to emerge in practice, limiting commercial viability despite the appeal of high energy density and improved safety.[18,19,41–47] Recent evaluations of solid-state Na systems suggest that hard carbon remains the most practically deployable anode material due to its interface compatibility and cycling stability.[48] These persistent issues point to an incomplete understanding of early-stage alkali metal deposition and motivate atomic-scale studies of nucleation and clustering on representative carbon surfaces.

Graphene, due to its exceptional electrical conductivity, chemical inertness, and structural similarity to the basal planes of graphite and hard carbon, serves as a relevant and widely adopted model for carbon-based battery anodes.[22,25,26,28–30,49,50] While pristine graphene exhibits weak interactions with alkali metals (Li, Na, and K), intrinsic defects such as carbon vacancies (V_C), Stone–Wales rearrangements, and extended grain boundaries substantially alter local electronic and chemical reactivity.[22,51–53] These defects introduce localized states near the Fermi level, promoting partially covalent metal–carbon bonding and enabling the nucleation of metal clusters.[51,52,54–56] A range of defect and structural modifications have been explored as avenues for tuning alkali metal adsorption, including double vacancies, hydrogen-vacancy networks in graphane, and substitutional doping.[29,30,50] These strategies further underscore the broader relevance of defect engineering for tailoring metal–surface interactions in graphene and structurally analogous carbon anode materials.

Previous work has investigated the interactions of single alkali metal atoms (Li, Na, and K) with both pristine and defective graphene within MIBs.[29,56–59] These studies highlighted the important role played by intrinsic defects, particularly carbon vacancies (V_C), in single-ion binding and migration, identifying V_C as a primary source of irreversible capacity loss.[11,53,60,61] The metal–vacancy ($M–V_C$) binding is dominated by the strong interaction between the alkali metal and the unsaturated carbon dangling bonds, a feature common to all carbon vacancy-containing defects provided one or more dangling bonds remain.[49,59] Such localized interactions significantly enhance the stability and reduce the mobility of adsorbed metal atoms. Furthermore the V_C forms the simplest building block of many important defect clusters with other vacancies in the form of di-vacancy and extended defect pores and with hetero-atoms such as $(N_C)_nV_C$, $(O_C)_nV_C$ and as a result of doping. Other computational studies on lithium clustering demonstrated that small Li clusters adsorb more favorably on graphene compared to bulk Li metal surfaces,[54] exhibiting concentration-dependent binding energies that influence charging behavior.[62] Additionally, lattice-gas cluster expansion analyses have explored the equilibrium stability of Li coverages on graphene.[63] Despite these insights into lithium, corresponding studies addressing Na and K clustering remain limited, leaving significant gaps in understanding their nucleation behavior on graphene and motivating further systematic investigation.

Liang *et al.*[51] conducted a comparative study on Na clusters, showing that Na weakly adsorbs on pristine graphene but that double vacancies significantly enhance Na adsorption—a result aligned with our previous findings on defect-enhanced Na storage.[13,49,58,59] Collectively, these studies offer insights into the deposition and clustering of Li on graphene, though several questions remain. Experimental investigations into metallic Li nucleation on basal-plane graphene, for instance, indicate that the pristine surface is lithiophobic, with nucleation barriers too high to overcome,[52] whereas basal plane defects are believed to serve as nucleation sites, rendering the surface lithiophilic.[52] In practical MIB applications, such defects may arise from synthesis conditions or cycling-induced wear, linking them to suboptimal performance and non-ideal behavior. However, the role of defects remains largely undefined, posing an open question as to what drives Li and Na clustering tendencies, while K demonstrates no such effect.

This study systematically assesses the impact of a single vacancy on Li, Na, and K clustering behavior. Through density functional theory (DFT) calculations, we provide atomic-scale insights into M nucleation and cluster growth on graphene, for both pristine and vacancy systems. This approach offers a focused test case to elucidate the critical role of vacancy defects in M-clustering, clarifying the link between surface and cluster morphology and the propensity for dendrite formation.

2. Methodology

All density functional theory (DFT) calculations were performed spin-polarized using the CP2K code[64–68] at the Γ-point, employing DZVP-SR-MOLOPT basis sets[65] for valence electrons and GTH pseudopotentials[69–71] for core electrons. A plane-wave cutoff of 750 Ry and a relative cutoff of 60 Ry were used, yielding total energy convergence within 0.1 meV per formula unit. Initial defect-free relaxations were carried out on a 308-atom graphene supercell, generated *via* an 11 × 7 orthohexagonal expansion of the primitive cell (see Fig. S1 in the ESI†). For the pristine cell, both the in-plane lattice vectors and atomic positions were fully relaxed using the quasi-Newton BFGS algorithm.[72–75] In defect-containing calculations, only the atomic positions were optimized. A vacuum spacing of 25 Å was applied in the out-of-plane direction to eliminate spurious interlayer interactions.[66,68,76] The Perdew–Burke–Ernzerhof (PBE) functional[77,78] with D3-BJ dispersion corrections[79–83] was used, consistent with previous studies.[13,24,49,58,59,84,85] Geometry optimizations were deemed converged when the total energy changed by less than 1×10^{-7} eV and the maximum atomic force was below 0.005 eV $Å^{-1}$.

Using the lowest energy M adsorption sites previously identified in ref. 49, the lowest-energy cluster configurations were determined *via* a stepwise sampling scheme.[86] Starting with a single metal atom (M_1), atoms were sequentially added to form each M_{n+1} cluster from M_n. To efficiently identify sites where a significant M–M interaction occurs as a prerequisite for cluster growth, any incremental interaction energy greater than −0.05 eV is treated as negligible and therefore non-interacting with respect to cluster growth. In effect, for a given neighboring site, if $\Delta E \geq -0.05$ eV, the corresponding binding interaction is considered statistically insignificant, as this value is on the order of (or below) twice the thermal energy at ambient conditions ($k_BT \approx 0.025$ eV). Consequently, only sites exhibiting $\Delta E_{\text{pair}} \leq -0.05$ eV are included in the initial sampling. In practice the search space is constrained to those sites that are predicted to result in either lateral or vertical growth of the cluster. The total number of configurations considered at each iteration is given by

$$C_n = \prod_{i=1}^{n} S_i,$$

where S_i denotes the set of available neighboring sites for the i-th added metal atom that satisfy the criterion $\Delta E \geq -0.05$ eV. Our sampling scheme is designed to efficiently identify robust cluster formation—a necessary precursor to dendrite nucleation—by excluding weakly or non-interacting configurations (*i.e.*, those with $\Delta E \geq -0.05$ eV). By focusing on configurations where the incremental binding energy satisfies $\Delta E \leq -0.05$ eV, we target only those sites likely to yield significant lateral or vertical cluster growth. In the context of battery operation, stable cluster nucleation and growth are understood to correlate with inhomogeneous deposition and dendrite formation.

To evaluate nucleation behavior, interaction energies were calculated using three key metrics: the formation energy E_f, using Zhang and Northrup's standard formalism[87] (eqn (1)), the binding energy E_{bind} (eqn (2)), and the cohesive energy E_{coh} (eqn (3)):

$$E_f = \frac{E_{M_n@\text{surface}} - E_{\text{surface}} - n\mu_M}{n}, \quad (1)$$

$$E_{\text{bind}} = \frac{E_{M_n@\text{surface}} - E_{\text{surface}} - E_{M_n}}{n}, \quad (2)$$

$$E_{\text{coh}} = \frac{E_{M_n} - n\mu_M}{n}, \quad (3)$$

where $E_{M_n@\text{surface}}$ is the total energy of the M_n cluster adsorbed on the graphene surface, E_{surface} is the energy of the reference surface—either pristine or containing a single carbon vacancy (V_C)—and n is the number of metal atoms in the cluster. The chemical potential μ_M is taken as the energy of an isolated neutral atom in vacuum; E_f and E_{coh} calculated with μ_M from bulk metal values are reported in the ESI Fig. S2 and S21† for reference.

The formation energy E_f quantifies the average energetic cost of assembling the adsorbed cluster from isolated atoms. The binding energy E_{bind} captures the net interaction between the cluster and the surface, where negative values indicate attractive interactions and positive values imply repulsion. The cohesive energy E_{coh} describes the intrinsic metal–metal bonding within the cluster in vacuum; more negative values correspond to stronger cohesion. These metrics are interdependent. In particular, strong metal–surface interactions (large negative E_{bind}) often weaken intra-cluster cohesion (less negative E_{coh}) due to geometric or electronic frustration. This antagonistic relationship provides insight into whether cluster formation is favored over dispersion.

Thermodynamic stability was further assessed using the incremental formation energy relative to the M_1 representing a disperse coverage with no M–M interactions:

$$\Delta E_f = E_f(n) - E_f(n = 1). \quad (4)$$

Clusters with $\Delta E_f < 0$ are energetically favored to form and grow, whereas $\Delta E_f > 0$ implies instability and the clustering is unfavoured with respect to the disperse coverage. Note that kinetic effects are not considered in this analysis. For consistency with prior studies, free-energy corrections are omitted here, although several works[62,88–90] have extended energy-based analyses to incorporate entropic and zero-point contributions. All structural visualizations were prepared using VESTA.[91]

We employ two complementary approaches to elucidate the evolution of the charge transfer. First, we analyze the local coordination environment of the metal atoms by applying directional filtering to classify atoms based on their bonding configurations. This enables us to group metal atoms into distinct categories, such as those with surface coordination or those bonded only to other metal atoms, and to compute the average partial charges within each group as a function of cluster size. Second, we compute the total metal charge Q_{total} by summing the Mulliken charges[92] of all metal atoms in a cluster:

$$Q_{\text{total}}(n) = \sum_{i \in M_n} q_i, \quad (5)$$

where q_i is the Mulliken charge on the i-th metal atom, and n is the total number of metal atoms in the cluster. The ideal ionic limit is defined as nq_1, where q_1 is the charge of a single isolated metal atom, extracted from pristine M_1 systems *via* the oxidation reaction $M^0 \rightarrow M^+$. To quantify deviations from full ionic electron transfer, we introduce the fractional ionic character,

$$f(n) = \frac{Q_{\text{total}}(n)}{nq_1}, \quad (6)$$

which serves as a descriptor for the balance between electrons transferred to the surface and those retained within the cluster due to metal–metal bonding. By comparing results for pristine and vacancy-modified systems across Li, Na, and K, we provide a comprehensive analysis that correlates the average partial charge behavior with overall electron transfer characteristics as a function of cluster size. These trends are visualized using charge density difference plots to illustrate the spatial redistribution of electrons upon cluster formation. In these plots, the charge density difference $\Delta\rho(\mathbf{r})$ is calculated as

$$\Delta\rho(\mathbf{r}) = \rho_{\text{combined}}(\mathbf{r}) - \sum_i \rho_i(\mathbf{r}), \quad (7)$$

where $\rho_{\text{combined}}(\mathbf{r})$ is the total electron density of the combined system (*e.g.*, the M_n cluster on graphene), and $\rho_i(\mathbf{r})$ are the electron densities of the isolated components calculated in the same geometry. Regions with $\Delta\rho(\mathbf{r}) > 0$ indicate electron accumulation (electron gain), while regions with $\Delta\rho(\mathbf{r}) < 0$ indicate electron depletion (electron loss).

3. Results and discussion

To investigate metal (M) nucleation and clustering on graphene, we systematically examine two systems: (1) the pristine basal plane providing our defect-free reference, and (2) the basal plane containing a carbon vacancy (V_C). This comparative approach addresses the following key question: How does the presence of a V_C defect impact the binding energy (E_{bind}) and cohesive energy (E_{coh}) of metal clusters, and consequently, the morphology and stability of the clusters? By analyzing these systems the role of defect-induced surface modifications in promoting or suppressing metal clustering is elucidated.

3.1. Metal clustering on the pristine basal plane: trends in stability and morphology

To investigate the formation of M_n clusters (n = 1–12), we calculated the cluster binding energies on the defect-free graphene basal plane. E_{bind}, E_{coh}, and E_f are shown in Fig. 1, along with the associated cluster geometries. In all cases, the isolated metal atom preferentially adsorbs at the hole site (above the centre of the C_6 ring), consistent with previous studies.[29,49,93,94] For clusters with $n \geq 2$, short-range M–M repulsive interactions distort the geometry, displacing metal atoms from the high-symmetry adsorption site. The degree of distortion is dictated by the inter-site distance between neighbouring hole sites (2.46 Å) in the graphene basal plane and the extent to which M–M separations can be accommodated on the carbon surface.

For Li_2 (Fig. 1a and d), the addition of a second Li atom to Li_1 induces a notable distortion, with a Li–Li separation of 3.12 Å. This displacement from the high-symmetry site (0.33 Å) leads to a number of Li–C bond lengths, replacing the single bond observed in the Li_1 (Fig. 2a). Na_2 adopts a similar configuration to Li_2 but with a greater distortion (3.47 Å) (Fig. 1b), reflecting the larger ionic radius of Na. The increased displacement gives the Na_2 significant top-site character, driving an increase in the Na–C bond length (Fig. 2b). In contrast, K_2 shows greater relaxation than either Li or Na, relaxing into a configuration with atoms located at distorted next-next-nearest-neighbour hole sites (Fig. 1c). No stable neighbour or next-neighbour minima were found without applying constraints; upon releasing the constraint, the system relaxed to the next-next-neighbour geometry, corresponding to a K–K separation of 7.86 Å (Fig. 2c).

For all Li_1 and Li_2 configurations, the dominant interaction is between the metal atom and the surface, as reflected by charge transfer trends (Fig. 3a–c). As previously reported, adsorption of an isolated metal atom results in the transfer of its valence s-electron to the underlying C_6 ring, following the reaction:

$$M^0 + C_6^0(\text{graphene}) \rightarrow M^+ + C_6^-(\text{graphene}),$$

which is captured by Mulliken charges of $0.7–0.85e^-$ on the metal and visualised in the $\Delta\rho(\mathbf{r})$ plots (Fig. S12–S14 in the ESI†).[49] This picture remains valid for K_2, but for Li_2 and Na_2, the presence of a second metal atom leads to a significant reduction in the net positive charge, with Mulliken charges dropping to $0.5e^-$ and $0.4e^-$, respectively (Fig. 3).

The reduction in partial charge arises from the emergence of partially occupied metal states at the Fermi energy, as shown in

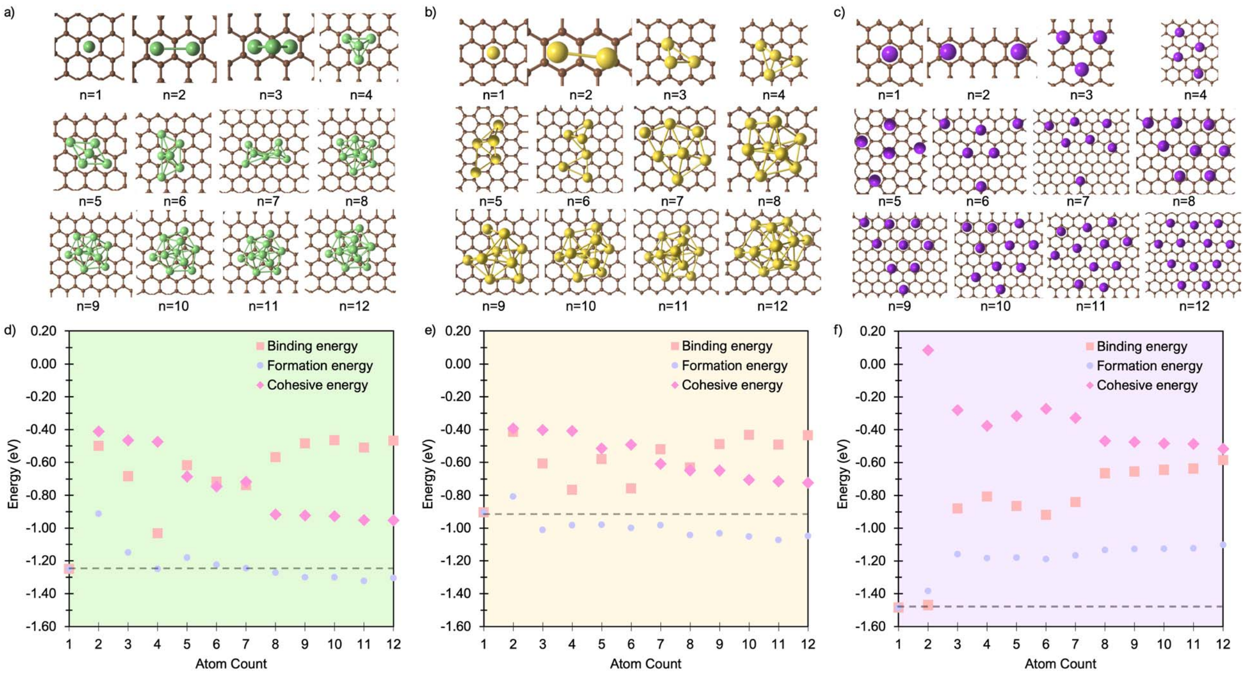

Fig. 1 Lowest energy cluster configurations on the pristine basal plane for (a) Li (green spheres represent Li atoms and brown spheres represent C atoms), (b) Na (yellow spheres represent Na atoms), and (c) K (purple spheres represent K atoms). Side views of the lowest energy cluster configurations are included in the ESI (Fig. S3–S5).† The interaction energies decomposed into binding energy (E_{bind}), cohesive energy (E_{coh}), and formation energy (E_f) are plotted for Li in (d), Na in (e), and K in (f), with the atom count denoting the number of M atoms in the M_n clusters.

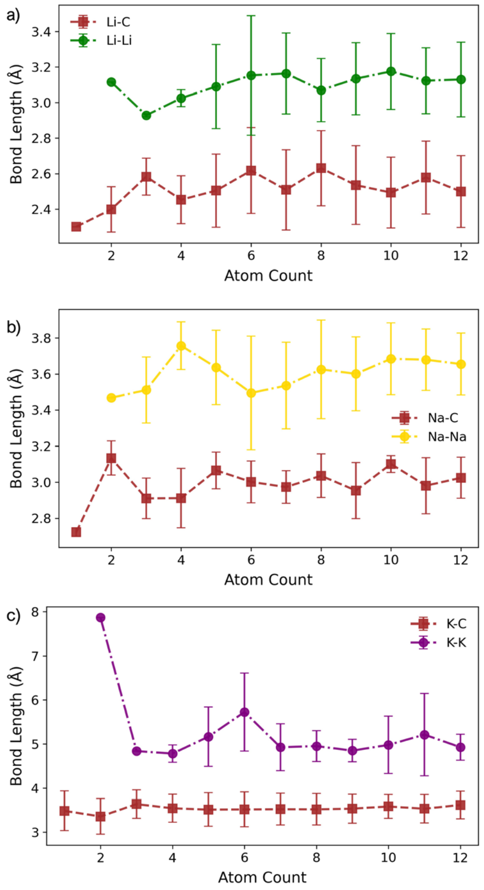

Fig. 2 Bond lengths as a function of M cluster size (atom count) for (a) Li, (b) Na, and (c) K clusters on the pristine basal plane, showing the C–M and M–M distances.

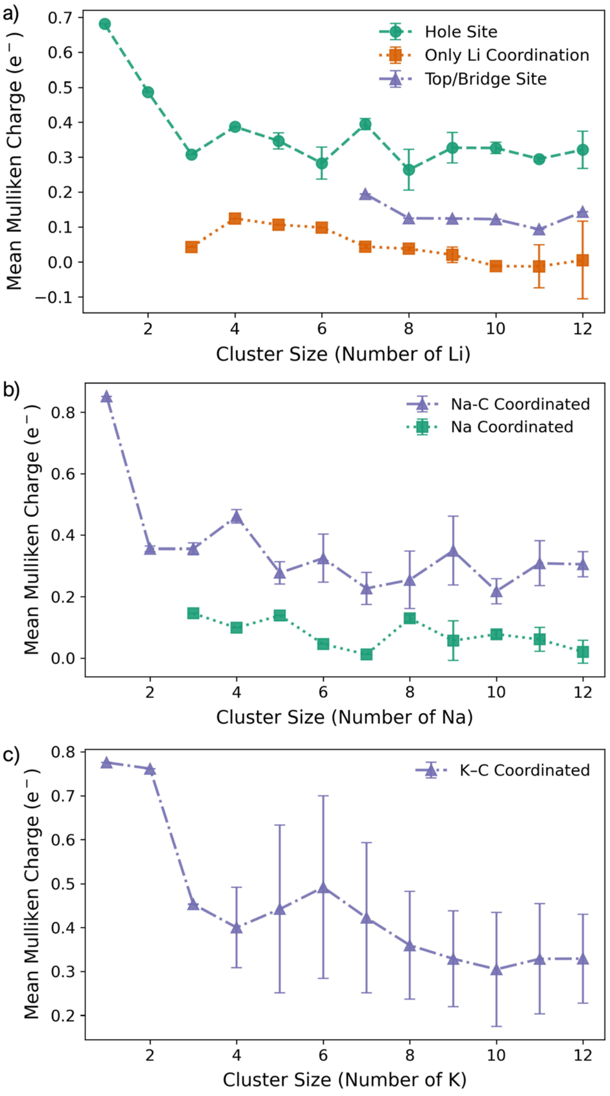

Fig. 3 Mean Mulliken charges as a function of M cluster size for (a) Li, (b) Na, and (c) K clusters on the pristine basal plane.

the projected density of states (PDOS) (Fig. S11 in the ESI†), and from charge redistribution between the metal centres, evident in the $\Delta\rho(\mathbf{r})$ plots (Fig. S12–S14 in the ESI†). Energetically, M_2 formation is unfavoured in all cases, with ΔE_f of +0.34 eV per atom for Li_2, +0.05 eV per atom for Na_2, and no stable configuration identified for K_2; even the relaxed next-next-neighbour geometry remains +0.15 eV per atom higher in energy than the K_1. While E_{coh} for both Li_2 and Na_2 is moderately stabilising at −0.40 eV per atom, it is insufficient to counteract the ~50% reduction in E_{bind} relative to the M_1 reference (Fig. 1d and e).

For K_3, the trends described previously continue, with two important differences (Fig. 1f). Firstly, E_{coh} becomes negative (−0.2 eV per atom), indicating the onset of an attractive K–K interaction. The K–K separation is reduced to 4.8 Å, with next-neighbour top sites occupied (Fig. 2c). Secondly, as observed for Li_2 and Na_2, the attractive interaction is driven by the emergence of K-derived states at the Fermi energy (Fig. S11 in the ESI†), which in turn leads to a notable reduction in partial charge (Fig. 3c and S14 in the ESI†).

In contrast, the behaviour of Li_3 and Na_3 differs markedly. In both cases, the M_2 configuration is preserved, with the additional metal atom binding preferentially to the existing metal ions, without direct interaction with the carbon surface (Fig. 1a and b). The influence of M–M interactions is pronounced. Firstly, there is a significant decrease in the M–M bond lengths (Fig. 2b and c), due to the absence of meaningful geometric constraints from the surface lattice. Secondly, E_{coh} becomes substantially more favourable for both Li and Na (Fig. 1d and e), while E_{bind} remains comparable to that of the dimer, indicating that the energetic benefit arises primarily from the metal–metal interaction.

Finally, analysis of the partial charges reveals the presence of two distinct coordination environments: cationic, surface-adsorbed metal ions (as observed for M_2), and metal-coordinated sites with no direct C-interaction. The trend established with Li_2 continues, with a further reduction in the partial charge to $0.33e^-$ for surface-bound sites, accompanied by an increased density of Li states at the Fermi level. For Na_3, the partial charges and associated electronic states remain essentially unchanged relative to Na_2, indicating that no additional charge redistribution occurs. It is noteworthy that the total reduction in partial charge from Li_1 to Li_3 mirrors that observed between Na_1 and Na_2, *via* the intermediate Li_2 configuration. For both Li and Na, the metal-coordinated sites are electronically distinct, exhibiting near-neutral character: approximately $0e^-$ for Li and $0.2e^-$ for Na (Fig. 3, S12 and S13 in the ESI†). Despite the onset of attractive interactions, cluster formation at $n = 3$ remains strongly disfavoured for Li and K, with ΔE_f values of +0.20 eV per atom and +0.22 eV per atom, respectively. In contrast, Na cluster formation becomes energetically favourable at this size, with $\Delta E_f = -0.11$ eV per atom.

The formation of M_4 clusters marks the point at which the clustering behaviour begins to diverge significantly between the metals. For Li, Li_4 forms *via* lateral addition to an adjacent hole site, accompanied by relaxation of the previously Li-coordinated atom into the central threefold symmetry site. This structure serves as the fundamental building block for larger clusters, with subsequent growth proceeding by lateral addition to distorted hole, top, or bridge sites (depending on size), followed by vertical growth through the Li-coordinated site. This stepwise occupation is illustrated in Fig. S3 in the ESI.† The mean Li–Li and Li–C bond lengths, shown in Fig. 2a, exhibit a gradual increase in Li–Li separation with cluster size, reaching a maximum spread at Li_6, where partial formation of a second layer occurs (see Fig. S6 and S7 in the ESI†). The introduction of the threefold-coordinated Li site has a notable effect on the electronic structure, introducing a state deep in the valence band and shifting the charge character towards a more neutral Li^0 configuration, as evident in Fig. 3 and visualised in the $\Delta\rho(\mathbf{r})$ plots (Fig. S12 in the ESI†).

As cluster size increases, the variation across sites of a given type also increases, reducing the precision with which associated geometric and charge-based descriptors can be defined. E_{coh} becomes markedly more favourable with increasing cluster size, although this is partially offset by a reduction in E_{bind}. Consequently, ΔE_f becomes increasingly favourable for cluster sizes $n > 7$, with the clustered and dispersed forms becoming energetically degenerate at $n = 4$ and $n = 7$. For lithium, this suggests that clustering can occur under high deposition rates, potentially contributing to the observed plating, with the nucleation probability distributed equally across a degenerate set of surface sites.[52]

Na follows a similar clustering pattern to Li, but with two important differences. Firstly, its larger ionic radius leads to a greater mismatch between the Na–Na bond length and the spacing between surface adsorption sites, resulting in a significantly larger distortion compared to Li (Fig. 2, S8 and S9 in the ESI†). Secondly, E_{bind} and E_{coh} exhibit substantial overlap, producing a fine balance between metal–metal and metal–carbon interactions (Fig. 1e).

While the general trends mirror those observed for Li, Na clusters consistently exhibit a marked degree of structural distortion at all sizes, a behaviour only seen in Li for the largest clusters ($n > 10$). This structural variability affects the electronic structure: instead of discrete states, the PDOS (Fig. S11 in the ESI†) appears smeared, reflecting the range of geometries present within each cluster. This in turn manifests in the partial charges, where the Na–C interactions span a wide range even in the smallest clusters. Unlike Li, these charges cannot be cleanly distinguished by adsorption site due to the relatively weaker binding of Na (Fig. 3b).

As previously noted, E_{coh} and E_{bind} lie within a narrow window of approximately 0.4 eV, with E_{coh} becoming gradually more favourable and E_{bind} increasingly less so as cluster size increases. The resulting formation energy, ΔE_f, indicates that cluster formation becomes energetically favourable for $n > 2$, with Na_2 already exhibiting a slightly positive ΔE_f of +0.05 eV per atom. This suggests that Na dendrite formation may occur even on pristine basal plane structures, consistent with experimental observations.[95–98] However, given the relatively weak binding energy of these Na clusters, further investigation is needed to determine whether they remain anchored to the surface or desorb as isolated entities.

K continues to form a single-layer structure, with atoms spaced to balance metal–metal repulsion against emerging lateral interactions. As the number of K atoms increases, there is a corresponding increase in the spread of K–K distances and the diversity of adsorption sites occupied (Fig. 2c). This variation in site occupancy and degree of lateral interaction leads to a range of partial charges, although the spread remains narrower than that observed for Li and Na, where vertical cluster growth occurs (Fig. 1c, S5 and S10 in the ESI†). Electronically, the behaviour remains consistent with that of K_3, showing an increase in the density of K-derived states as the cluster size increases. These states remain confined to the Fermi level and above, indicating no significant occupation of lower-energy states (Fig. S11 in the ESI†). Finally, although E_{coh} increases modestly with cluster size, this is more than offset by a corresponding decrease in the binding energy (E_{bind}). As a result, ΔE_f remains positive across all cluster sizes considered (Fig. 1f). This persistent absence of favourable K clustering supports the conclusion that K nucleation and dendrite formation are energetically unfavourable on pristine basal plane surfaces, consistent with experimental observations in carbon-based KIBs.[97,99,100]

In summary, the formation and stability of metal clusters on the pristine basal plane are governed by a delicate interplay between geometric accommodation, electronic delocalisation, and charge transfer. Li, Na, and K exhibit qualitatively distinct behaviours driven by their ionic radii and their ability to match the spatial periodicity of adsorption sites. Li forms compact clusters with clear layer-by-layer growth beyond $n = 3$, enabled by moderate geometric distortion and strong M–C binding. This growth leads to partial charge redistribution and the emergence of low-lying valence states, although cluster formation remains energetically unfavourable until $n \geq 7$. Na follows a similar motif, but its larger ionic size imposes greater geometric frustration, resulting in persistent distortion, smeared electronic states, and a complex distribution of partial charges. Despite these distortions, Na cluster formation becomes energetically favourable from $n = 3$, indicating a thermodynamic driving force for nucleation and potential dendrite formation, even in the absence of defects. In contrast, K displays fundamentally different behaviour: the weak M–C binding, strong M–M repulsion, and poor geometric compatibility inhibit both vertical growth and electron localisation. K remains in a dispersed monolayer configuration with minimal electronic perturbation and positive formation energies across all sizes, consistent with the absence of dendrite formation observed experimentally.[97,99,100]

Together, these results highlight how subtle differences in atomic size and metal–surface coupling give rise to distinct clustering pathways, offering mechanistic insight into the conditions under which metal dendrites may nucleate or be suppressed on carbon-based substrates.

3.2. Influence of carbon vacancies on metal clustering and stability

Building on the insights from pristine graphene, we now examine the influence of a single carbon vacancy (V_C) on metal cluster formation and stability. Fig. 4a–c presents the lowest-energy M_n cluster geometries on the V_C surface for Li, Na, and K (for side views, see Fig. S16–S18 in the ESI†). In all three cases, M_1 binds preferentially at the vacancy, coordinating to the under-coordinated carbon atom, while the remaining two carbons reconstruct to form a five-membered ring, consistent with earlier work on isolated metal adsorption.[49] The binding energies (Fig. 4d–f) at $n = 1$ are notably enhanced compared to pristine graphene (Fig. 1d–f), with E_{bind} values of −3.23 eV for Li, −2.52 eV for Na, and −2.84 eV for K. This enhancement reflects the strong interaction with the unsaturated carbon atom (Fig. 4a–c).

The corresponding M–C bond lengths, shown in Fig. 5, are significantly shorter than those in the pristine system (Fig. 2). This shift is driven by the formation of a strong M–C* bond, with distances of 2.03 Å, 2.36 Å, and 2.81 Å for Li_1, Na_1, and K_1, respectively. The presence of the dangling bond alters the charge transfer mechanism: the transferred charge is now predominantly localised on the under-coordinated carbon rather than delocalised over the C_6 ring (see Fig. S26–S28 in the ESI†). The reaction

$$C_1^0 + M^0 \rightarrow C_1^{\,-} + M^+$$

leads to a reduced metal partial charge in all cases (most dramatically for Li) indicating an increasingly covalent character to the metal–surface interaction (Fig. 6).

For M_2, the added atom occupies the adjacent vacancy hole site in the case of Li_2 and Na_2, and the next-neighbour hole site for K_2, with both metal centres interacting with the unsaturated carbon atom. The Li and Na atoms occupy equivalent sites and exhibit negligible extension relative to M_1 (M–C* distances: Li_2, 2.05 Å; Na_2, 2.36 Å) (Fig. 5a and b). In contrast, K_2 adopts a more asymmetric configuration, with one atom at the vacancy and the other on the next-neighbour hole site, giving K–C* distances of 2.81 Å and 3.68 Å, respectively (Fig. 5c). The partial charges (Fig. 6) remain largely consistent for Li_2, while Na_2 and K_2 exhibit a small decrease of approximately $0.1e^-$. In all cases, the charge transfer extends beyond the under-coordinated carbon to neighbouring C atoms, as shown in Fig. S26–S28 in the ESI.† Inspection of the PDOS (Fig. S25 in the ESI†) highlights a key distinction from the pristine system: the metal-derived states remain unoccupied and lie well above the Fermi level, whereas

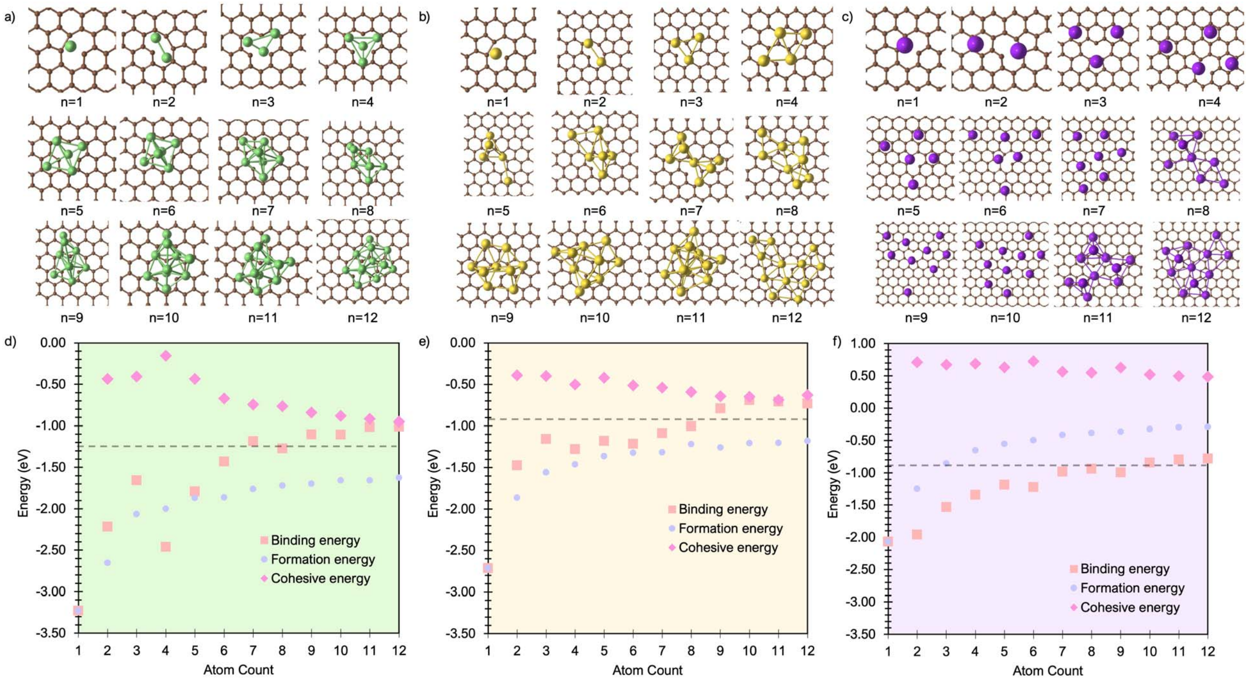

Fig. 4 Lowest energy cluster configurations on the defective basal plane for (a) Li (green spheres represent Li atoms and brown spheres represent C atoms), (b) Na (yellow spheres represent Na atoms), and (c) K (purple spheres represent K atoms). Side views of the lowest energy cluster configurations are included in the ESI (Fig. S16–S18).† The interaction energies decomposed into binding energy (E_{bind}), cohesive energy (E_{coh}), and formation energy (E_{f}) are plotted for Li in (d), Na in (e), and K in (f), with the atom count denoting the number of M atoms in the M_n clusters.

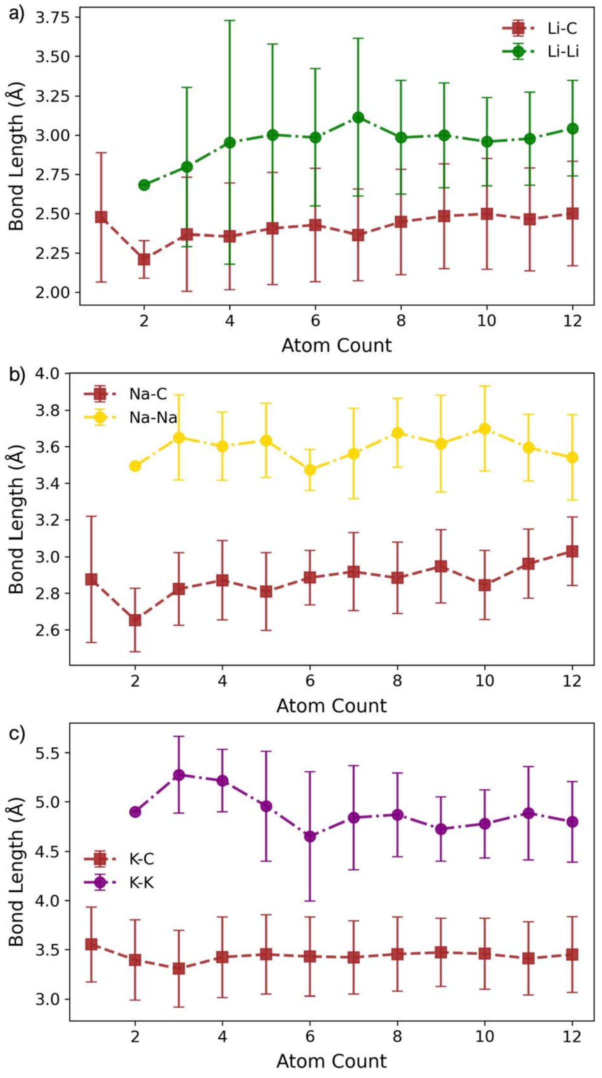

Fig. 5 Bond lengths as a function of M cluster size (atom count) for (a) Li, (b) Na, and (c) K clusters on the defective basal plane, showing the C–M and M–M distances.

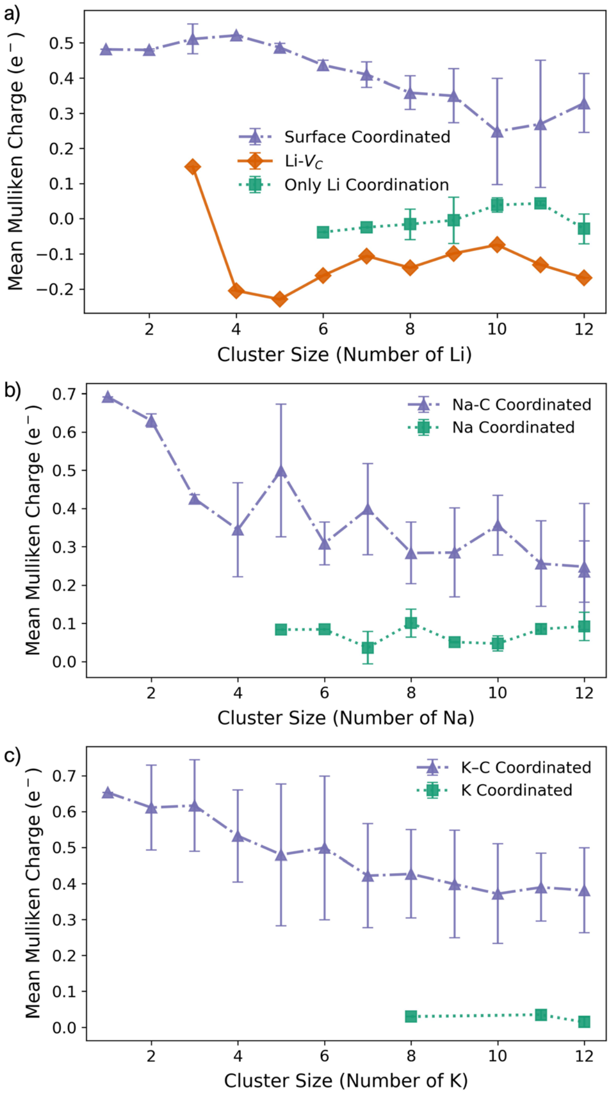

Fig. 6 Mean Mulliken charges as a function of M cluster size for (a) Li, (b) Na, and (c) K clusters on the defective basal plane. $\Delta\rho(\mathbf{r})$ plots are presented in Fig. S26–S28 in the ESI.†

in the pristine case, these states are partially filled. E_f is dominated by the strong binding of M_2 to the vacancy site (E_{bind}), although it is reduced compared to the M_1 case. E_{coh} is marginally more favourable than on the pristine surface, but its impact on ΔE_f is negligible (Fig. 4). All M_2 configurations remain strongly stabilised, with ΔE_f values of −1.2 eV per atom, −1.0 eV per atom, and −0.75 eV per atom for Li_2, Na_2, and K_2, respectively.

At M_3, Li exhibits markedly different behaviour. At Li_3, the five-membered carbon ring begins to open, with the C–C bond extending beyond 1.9 Å. This structural change is reflected in the partial charges (Fig. 6), where the Li atom interacting with the breaking C–C bond exhibits a significantly reduced Mulliken charge. At Li_4, the ring fully ruptures, enabling one Li atom to coordinate to three equivalent dangling carbon atoms with a short C–Li bond length of 1.85 Å. These under-coordinated carbon atoms are displaced upwards by approximately 1.2 Å from the graphene plane (Fig. 4a). The partial charge on this vacancy-bound Li site drops further $-0.1e^-$, while the Li atoms occupying nearby hole sites retain a consistent charge of $0.5e^-$ (Fig. 6a). Following this reconstruction, additional Li atoms preferentially occupy adjacent hole sites and, beyond Li_5, begin to adsorb vertically, initiating second-layer growth. This growth pathway mirrors that seen on the pristine surface, with the vacancy acting as an anchoring centre. The transition observed at Li_3 and Li_4 marks a shift from formation energy (E_f) dominated by strong metal–surface binding (E_{bind}) to one increasingly governed by metal–metal cohesion (E_{coh}). Beyond Li_4, E_{bind} becomes progressively less favourable with cluster size, while E_{coh} continues to increase. Nevertheless, all Li_n configurations remain energetically stabilised, with ΔE_f negative across the entire size range considered.

For both Na and K, the five-membered carbon ring (C_5) remains intact across all cluster sizes (Fig. 4b and c). For Na, clustering follows the same intermediate configurations as observed on the pristine surface, with small clusters ($n \leq 3$) anchored at the vacancy site, rendering their formation significantly more favourable. The presence of the vacancy leads to an increased spread in bond lengths (Fig. 5b) and partial charges (Fig. 6b), although the mean values remain comparable to those on the pristine surface. This broadened distribution arises from the combination of local distortion induced by the vacancy and the fixed nature of tightly bound atoms in the small clusters, which are energetically costly to displace. Consequently, additional atoms must accommodate these anchored positions, introducing greater structural distortion within the growing cluster, as illustrated schematically in Fig. S22 and S23 in the ESI.† The PDOS shows a similar trend to the pristine case: Na–Na interactions produce states degenerate with the Fermi level, while non-carbon-coordinated Na atoms contribute deeper-lying valence band states (Fig. S25 in the ESI†).

For all Na_n clusters considered, ΔE_f remains negative, indicating favourable clustering. As with Li, a gradual transition is observed from an initial regime dominated by strong local vacancy interactions (E_{bind}) to a regime where E_{coh} and E_{bind} contributions are of comparable magnitude, approaching the energetic balance seen on the pristine surface.

For K, clustering proceeds in a manner broadly similar to the pristine system, with two notable exceptions. First, there is a marked energetic antagonism between the vacancy-bound K atom and additional K atoms occupying non-vacancy sites during vertical growth. This competition results in favourable multilayer configurations emerging only at K_8, K_{11}, and K_{12}, though isoenergetic lateral configurations exist at each of these sizes. Second, the formation energy ΔE_f is negative only for clusters up to K_5, where the strong local vacancy interaction dominates. The comparatively weak E_{coh} of potassium limits the transition to a surface-anchored growth mode seen for both Li and Na. As a result, while the vacancy can stabilise small K_n clusters, it does not promote sustained growth. This reinforces the conclusion that potassium remains resistant to nucleation and dendrite formation, even in the presence of surface defects.

3.3. Discussion

The introduction of a carbon vacancy (V_C) dramatically alters the thermodynamics of metal clustering on the graphene basal plane. For all three metals, the presence of an unsaturated carbon at the vacancy enhances the local binding energy (E_{bind}) of the initial adsorbed atom, leading to stronger anchoring and the stabilisation of otherwise unfavourable small clusters. As cluster size increases, however, this effect becomes localised: the vacancy contribution is diluted on a per-atom basis, and E_{bind} converges toward the pristine values. Concurrently, E_{coh} grows steadily more favourable, approaching the bulk metal limit. This crossover from vacancy-dominated to cluster-internal energetics provides a natural scale for predicting cluster size thresholds for nucleation and vertical growth.

Geometrically, the vacancy site introduces a strong asymmetry that constrains early-stage cluster morphology. For Li, the vacancy drives a structural transformation: the five-membered ring opens at $n = 3$, enabling a central Li atom to coordinate to three under-coordinated carbon atoms at $n = 4$. This geometry stabilises the cluster and defines the onset of vertical growth. In contrast, Na and K preserve the five-membered ring across all cluster sizes. This rigidity, combined with the larger equilibrium M–M distances, limits the accessible surface adsorption geometries and restricts metal-carbon relaxation. These trends are mirrored in both the metal–carbon bond lengths and partial charge distributions: Li exhibits shorter bonds and enhanced covalent character at the vacancy, while Na and K maintain the single dangling bond interaction.

The evolution of the electronic structure reflects the transition from localised surface binding to collective metallic behaviour. For Li and Na, small clusters exhibit sharp distinctions in the PDOS, with surface-bound atoms contributing states near the Fermi level, while interior or second-layer atoms retain deeper-lying, metal-like character. This evolution is accompanied by a progressive reduction in Mulliken partial charge with increasing cluster size, consistent with charge delocalisation and the emergence of quasi-metallic behaviour. For Li, the partial charge on the vacancy-bound site drops from $\sim 0.5e^-$ at $n = 1$ to $\sim 0.1e^-$ at $n = 4$, and reaches $\sim -0.2e^-$ at $n = 5$. Na exhibits a more gradual reduction, with the vacancy-bound site stabilising near $\sim 0.2e^-$ by $n = 6$. In both cases, the emergence of metal-derived states degenerate with the Fermi level coincides with lateral metal–metal interaction, while vertical growth introduces deeper-lying valence band states associated with non-surface-bound atoms.

To further quantify the interplay between electron transfer and cluster growth, we calculate the total cluster charge Q_{total} (Fig. 7a–c) and the fractional ionic character $f(n)$ (Fig. 7d–f). Q_{total} represents the summed Mulliken charge of all metal atoms in a given cluster, while $f(n) = Q_{total}/(nq_1)$ normalizes this value relative to the ideal ionic limit, defined by the charge q_1 of the isolated surface adsorbed metal (M_1). For all metals on the pristine surface, Q_{total} increases sublinearly with n, indicating a progressive departure from predominantly ionic behavior (Fig. 7a–c). This deviation is most pronounced for Li and Na, where $f(n)$ drops rapidly from unity to approximately 0.3 by $n =$ 6–8, consistent with the emergence of strong metal–metal bonding within the cluster (Fig. 7d and e). In contrast, K exhibits weaker charge transfer overall, with $f(n)$ remaining above 0.4 even at the largest cluster sizes studied (Fig. 7f). The presence of a carbon vacancy primarily influences the smallest clusters ($n = 1$–3), where electron transfer is enhanced through interaction with the vacancy's dangling bond. At $n = 1$, $f(n)$ increases to 0.71, 0.82, and 0.85 for Li, Na, and K respectively. However, beyond $n = 4$, the influence of the vacancy saturates, and $f(n)$ converges toward the pristine trend. These trends confirm that electron donation to the surface is rapidly exhausted, and that beyond a critical cluster size, excess charge remains within the cluster itself – consistent with the development of delocalized metallic states near, and eventually below, the Fermi level (Fig. S11 and S25 in the ESI†). Importantly, the vacancy has only a modest effect on $f(n)$ beyond the smallest sizes, reinforcing its role as a local defect that governs early-stage nucleation without significantly altering the longer-range electronic character of the cluster.

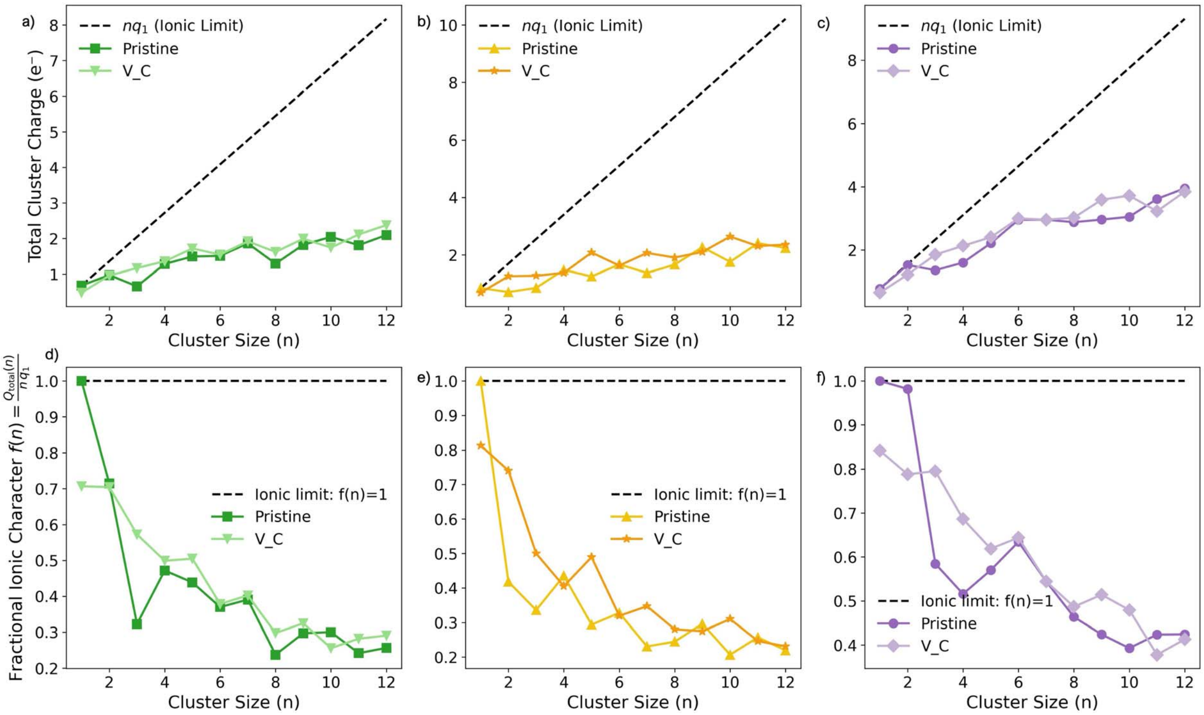

Fig. 7 Total metal cluster charge (Q_{total}) for (a) Li, (b) Na, and (c) K, and their fractional character (*f*(*n*)) for (d) Li, (e) Na, and (f) K.

Overall, these findings highlight the dual role of carbon vacancies in mediating early-stage metal nucleation. Vacancies not only stabilise small clusters that are otherwise unfavourable on pristine graphene, but also imprint distinct structural and electronic fingerprints on the growing ensemble. The vacancy acts as an anchor point, localising charge and stabilising low-coordinate geometries, while facilitating a controlled transition to extended, metallic clusters through lateral and vertical addition. The extent to which this anchoring effect persists depends sensitively on the balance between vacancy–metal binding, metal–metal cohesion, and the geometric constraints imposed by ionic radius. As a result, the vacancy-driven nucleation landscape is element-specific: Li benefits from strong, directional bonding and cohesive growth; Na occupies an intermediate regime where distortion accommodates nucleation; and K remains largely non-nucleating, even with defect assistance. These distinctions offer a predictive framework for interpreting alkali metal behaviour on defective carbon and for designing anode materials that control clustering through tailored surface chemistry.

4. Conclusions

This study systematically examines the nucleation and growth of Li, Na, and K clusters on both pristine graphene and defective surfaces featuring a single carbon vacancy (V_C), elucidating the thermodynamic pathways underlying dendrite formation in alkali metal-ion batteries.

On the pristine basal plane, cluster growth is hindered for Li due to strong M–M repulsion and the unfavourable energetics of small clusters. K exhibits minimal clustering across all sizes, reflecting its weak binding and large ionic radius. In contrast, Na clusters readily form, with ΔE_f becoming favourable as early as $n = 3$, suggesting an inherent propensity for dendrite nucleation even in the absence of defects. The introduction of a vacancy site dramatically alters this picture. For Li, the V_C stabilises otherwise unstable small clusters, enabling stepwise growth anchored at the defect. For Na, already favourable clustering is further enhanced by the vacancy, reinforcing inhomogeneous nucleation pathways. K, while weakly bound overall, shows modest cluster stabilisation at small sizes, but fails to achieve favourable vertical growth, maintaining resistance to dendrite formation.

These behaviours arise from the interplay between metal–carbon binding, metal–metal cohesion, and electronic structure evolution, with the vacancy shifting the balance from surface-limited to metal-dominated growth. Importantly, the findings reveal that even a single point defect can serve as a nucleation hotspot, transforming otherwise uniform growth into spatially heterogeneous clustering. Given the diversity of intrinsic and extrinsic defects in real carbonaceous anodes, extending this analysis beyond vacancies will be essential. Such insights will inform strategies for defect-engineered electrode design aimed at suppressing dendrite formation and enhancing long-term electrochemical stability.

Data availability

Data for this article are available at Zenodo at **https://doi.org/10.5281/zenodo.14747737**.

Conflicts of interest

There are no conflicts to declare.

Acknowledgements

This work was conducted at the Advanced Research Center for Nanolithography, a public-private partnership between the University of Amsterdam (UvA), Vrije Universiteit Amsterdam (VU), Rijksuniversiteit Groningen (RUG), the Netherlands Organization for Scientific Research (NWO), and the semiconductor equipment manufacturer ASML. This work made use of the Dutch national e-infrastructure with the support of the SURF Cooperative using grant no. EINF-2434 and EINF-5451. The authors thank SURF (**https://www.surf.nl/**) for the support in using the Lisa Compute Cluster and National Supercomputer Snellius. Q. C. would like to acknowledge funding support from the Faraday Institution through the LiSTAR programme (FIRG014, Grant FIRG083), and funding support from Horizon Europe *via* the OPERA consortium (Grant No. 101103834) under the UK Research and Innovation (UKRI)'s Horizon Europe funding guarantee (Grant No. 10078555). E. O. is grateful for a WISE Fellowship from the NWO and support *via* Holland High Tech through a public–private partnership in research and development within the Dutch top sector of High-Tech Systems and Materials (HTSM).

References

1 M. Armand and J. M. Tarascon, Building better batteries, *Nature*, 2008, **451**, 652.

2 K. Yuan, Y. Lin, X. Li, Y. Ding, P. Yu, J. Peng, J. Wang, H. K. Liu and S. Dou, High-Safety Anode Materials for Advanced Lithium-Ion Batteries, *Energy Environ. Mater.*, 2024, **7**(5), e12759.

3 S. Tagliaferri, L. Gaspard, H. Au, C. Mattevi, M. M. Titirici and M. Crespo-Ribadeneyra, Nature-inspired batteries: from biomaterials to biomimetic design strategies, *Green Chem.*, 2024, **26**, 6944.

4 M. Titirici, S. G. Baird, T. D. Sparks, S. M. Yang, A. Brandt-Talbot, O. Hosseinaei, D. P. Harper, R. M. Parker, S. Vignolini, L. A. Berglund, Y. Li, H. L. Gao, L. B. Mao, S. H. Yu, N. Díez, G. A. Ferrero, M. Sevilla, P. Ã. Szilágyi, C. J. Stubbs, J. C. Worch, Y. Huang, C. K. Luscombe, K. Y. Lee, H. Luo, M. J. Platts, D. Tiwari, D. Kovalevskiy, D. J. Fermin, H. Au, H. Alptekin, M. Crespo-Ribadeneyra, V. P. Ting, T. P. Fellinger, J. Barrio, O. Westhead, C. Roy, I. E. Stephens, S. A. Nicolae, S. C. Sarma, R. P. Oates, C. G. Wang, Z. Li, X. J. Loh, R. J. Myers, N. Heeren, A. Grégoire, C. Périssé, X. Zhao, Y. Vodovotz, B. Earley, G. Finnveden, A. Björklund, G. D. Harper, A. Walton and P. A. Anderson, The sustainable materials roadmap, *JPhys Mater.*, 2022, **5**, 032001.

5 N. Tapia-Ruiz, A. R. Armstrong, H. Alptekin, M. A. Amores, H. Au, J. Barker, R. Boston, W. R. Brant, J. M. Brittain, Y. Chen, M. Chhowalla, Y. S. Choi, S. I. Costa, M. C. Ribadeneyra, S. A. Cussen, E. J. Cussen, W. I. David, A. V. Desai, S. A. Dickson, E. I. Eweka, J. D. Forero-Saboya, C. P. Grey, J. M. Griffin, P. Gross, X. Hua, J. T. Irvine, P. Johansson, M. O. Jones, M. Karlsmo, E. Kendrick, E. Kim, O. V. Kolosov, Z. Li, S. F. Mertens, R. Mogensen, L. Monconduit, R. E. Morris, A. J. Naylor, S. Nikman, C. A. O'Keefe, D. M. Ould, R. G. Palgrave, P. Poizot, A. Ponrouch, S. Renault, E. M. Reynolds, A. Rudola, R. Sayers, D. O. Scanlon, S. Sen, V. R. Seymour, B. Silván, M. T. Sougrati, L. Stievano, G. S. Stone, C. I. Thomas, M. M. Titirici, J. Tong, T. J. Wood, D. S. Wright and R. Younesi, 2021 roadmap for sodium-ion batteries, *JPhys Energy*, 2021, **3**, 031503.

6 A. Eftekhari and D. W. Kim, Sodium-ion batteries: New opportunities beyond energy storage by lithium, *J. Power Sources*, 2018, **395**, 336–348.

7 H. Au, M. Crespo-Ribadeneyra and M.-M. Titirici, Beyond Li-ion batteries: performance, materials diversification, and sustainability, *One Earth*, 2022, **5**, 207.

8 J. Zhang, X. Yao, R. K. Misra, Q. Cai and Y. Zhao, Progress in electrolytes for beyond-lithium-ion batteries, *J. Mater. Sci. Technol.*, 2020, **44**, 237.

9 R. C. Massé, E. Uchaker and G. Cao, Beyond Li-ion: electrode materials for sodium- and magnesium-ion batteries, *Sci. China Mater.*, 2015, **58**, 715.

10 W. Li, H. Wang, E. Matios and J. Luo, Combining theories and experiments to understand the sodium nucleation behavior towards safe sodium metal batteries, *Chem. Soc. Rev.*, 2020, **49**, 3783.

11 H. Au, H. Alptekin, A. C. S. Jensen, E. Olsson, C. A. O'Keefe, T. Smith, M. Crespo-Ribadeneyra, T. F. Headen, C. P. Grey, Q. Cai, A. J. Drew and M.-M. M. Titirici, A revised mechanistic model for sodium insertion in hard carbons, *Energy Environ. Sci.*, 2020, **13**, 3469.

12 S. Chen, T. Hu, T. Yu, X. Luo, L. Zhang and F. Li, Structural Feature Design for Carbon Materials toward Sodium Storage: Insights and Prospects, *ACS Energy Lett.*, 2025, **10**(4), 1931–1952.

13 E. Olsson, J. Cottom, H. Au, Z. Guo, A. C. S. Jensen, H. Alptekin, A. J. Drew, M.-M. Titirici and Q. Cai, Elucidating the Effect of Planar Graphitic Layers and Cylindrical Pores on the Storage and Diffusion of Li, Na, and K in Carbon Materials, *Adv. Funct. Mater.*, 2020, **30**, 1908209.

14 E. Buiel and J. R. Dahn, Li-insertion in hard carbon anode materials for Li-ion batteries, *Electrochim. Acta*, 1999, **45**, 121.

15 L. F. Zhao, Z. Hu, W. H. Lai, Y. Tao, J. Peng, Z. C. Miao, Y. X. Wang, S. L. Chou, H. K. Liu and S. X. Dou, Hard Carbon Anodes: Fundamental Understanding and Commercial Perspectives for Na-Ion Batteries beyond Li-Ion and K-Ion Counterparts, *Adv. Energy Mater.*, 2021, **11**, 1.

16 R. A. Adams, A. Varma and V. G. Pol, Carbon Anodes for Nonaqueous Alkali Metal-Ion Batteries and Their Thermal Safety Aspects, *Adv. Energy Mater.*, 2019, **9**, 1900550.

17 Y. Li, Y. Lu, P. Adelhelm, M.-M. Titirici and Y.-S. Hu, Intercalation chemistry of graphite: alkali metal ions and beyond, *Chem. Soc. Rev.*, 2019, **48**, 4655.

18 J. Xiao, N. Xiao, K. Li, L. Zhang, J. Chang, X. Ma, H. Li, J. Bai, Q. Jiang and J. Qiu, Ultra-High Fluorine Enhanced Homogeneous Nucleation of Lithium Metal on Stepped Carbon Nanosheets with Abundant Edge Sites, *Adv. Energy Mater.*, 2022, **12**, 2103123.

19 F. Flatscher, J. Todt, M. Burghammer, H. S. Søreide, L. Porz, Y. Li, S. Wenner, V. Bobal, S. Ganschow, B. Sartory, R. Brunner, C. Hatzoglou, J. Keckes and D. Rettenwander, Deflecting Dendrites by Introducing Compressive Stress in Li7La3Zr2O12 Using Ion Implantation, *Small*, 2024, **20**, 2307515.

20 R. Mukherjee, A. V. Thomas, D. Datta, E. Singh, J. Li, O. Eksik, V. B. Shenoy and N. Koratkar, Defect-induced plating of lithium metal within porous graphene networks, *Nat. Commun.*, 2014, **5**, 3710.

21 A. Rajkamal and R. Thapa, Carbon Allotropes as Anode Material for Lithium-Ion Batteries, *Adv. Mater. Technol.*, 2019, **4**, 1900307.

22 E. Olsson, J. Yu, H. Zhang, H. Cheng and Q. Cai, Atomic-Scale Design of Anode Materials for Alkali Metal (Li/Na/K)-Ion Batteries: Progress and Perspectives, *Adv. Energy Mater.*, 2022, **12**, 2200662.

23 Y. Li, Y. Lu, P. Adelhelm, M.-M. Titirici and Y.-S. Hu, Intercalation chemistry of graphite: alkali metal ions and beyond, *Chem. Soc. Rev.*, 2019, **48**, 4655.

24 S. Payá, N. Díez, J. Cottom, E. Olsson and M. Sevilla, MgSO4 as an Effective, Low-Temperature Sulfur Dopant for Carbon Materials Enabling Fast Sodium Storage, *ACS Appl. Energy Mater.*, 2024, **7**, 10061.

25 M. S. Balogun, Y. Luo, W. Qiu, P. Liu and Y. Tong, A review of carbon materials and their composites with alloy metals for sodium ion battery anodes, *Carbon*, 2016, **98**, 162.

26 J. C. Pramudita, D. Sehrawat, D. Goonetilleke and N. Sharma, An Initial Review of the Status of Electrode Materials for Potassium-Ion Batteries, *Adv. Energy Mater.*, 2017, **7**, 1602911.

27 Y. Han, Y. Ni, X. Guo and T. Jiao, Insights into the mechanism of electric field regulating hydrogen adsorption on Li-functionalized N-doped defective graphene: A first-principles perspective, *Fuel*, 2024, **357**, 129655.

28 E. Olsson, T. Hussain, A. Karton and Q. Cai, The adsorption and migration behavior of divalent metals (Mg, Ca, and Zn) on pristine and defective graphene, *Carbon*, 2020, **163**, 276.

29 R. E. Mapasha, S. P. Kgalema, H. Mapingire and E. Igumbor, Lithium on CH Divacancy Self-Healed Graphane: A First-Principles Study, *Nanoenergy Adv.*, 2024, **4**, 122–132.

30 S. P. Kgalema, M. Diale, E. Igumbor and R. E. Mapasha, Enhancement of lithiation on a graphane monolayer through extended H vacancy pathways: An ab initio study, *Phys. B*, 2024, **673**, 415490.

31 Q. Wang, H. Sun, Q. Li, X. Yang, W. Chen, J. Yan, Y. Lyu, G. Yan, H. Zhao, Z. Meng, Z. Yang and Y. Wang, Enhanced hydrogen storage in K and Na decorated DHP-graphene monolayer: DFT and GCMC study, *Chem. Phys. Lett.*, 2025, **865**, 141932.

32 W. Cai, Y.-X. Yao, G.-L. Zhu, C. Yan, L.-L. Jiang, C. He, J.-Q. Huang and Q. Zhang, A review on energy chemistry of fast-charging anodes, *Chem. Soc. Rev.*, 2020, **49**, 3806.

33 T. Liu, J. P. Vivek, E. W. Zhao, J. Lei, N. Garcia-Araez and C. P. Grey, Current Challenges and Routes Forward for Nonaqueous Lithium-Air Batteries, *Chem. Rev.*, 2020, **120**, 6558.

34 B. J. Landi, M. J. Ganter, C. D. Cress, R. A. DiLeo and R. P. Raffaelle, Carbon nanotubes for lithium ion batteries, *Energy Environ. Sci.*, 2009, **2**, 638.

35 L. M. Morgan, M. P. Mercer, A. Bhandari, C. Peng, M. M. Islam, H. Yang, J. Holland, S. W. Coles, R. Sharpe, A. Walsh, B. J. Morgan, D. Kramer, M. S. Islam, H. E. Hoster, J. S. Edge and C.-K. Skylaris, Pushing the boundaries of lithium battery research with atomistic modelling on different scales, *Prog. Energy*, 2022, **4**, 012002.

36 W. Liu, P. Liu and D. Mitlin, Review of Emerging Concepts in SEI Analysis and Artificial SEI Membranes for Lithium, Sodium, and Potassium Metal Battery Anodes, *Adv. Energy Mater.*, 2020, **10**, 2002297.

37 F. Wu, J. Maier and Y. Yu, Guidelines and trends for next-generation rechargeable lithium and lithium-ion batteries, *Chem. Soc. Rev.*, 2020, **49**, 1569.

38 S. Moharana, G. West, M. Walker, X. S. Yan and M. Loveridge, Controlling Li Dendritic Growth in Graphite Anodes by Potassium Electrolyte Additives for Li-Ion Batteries, *ACS Appl. Mater. Interfaces*, 2022, **14**, 42078.

39 X. Yao, *Interface Engineering and Advanced Characterisation for Solid-State Li Metal Batteries*, 2022.

40 J. Wang, Q. Ma, S. Sun, K. Yang, Q. Cai, E. Olsson, X. Chen, Z. Wang, A. M. Abdelkader, Y. Li, W. Yan, S. Ding and K. Xi, Highly aligned lithiophilic electrospun nanofiber membrane for the multiscale suppression of Li dendrite growth, *eScience*, 2022, **2**, 655.

41 G. Li and C. W. Monroe, Dendrite nucleation in lithium-conductive ceramics, *Phys. Chem. Chem. Phys.*, 2019, **21**, 20354.

42 X. Xing, Y. Li, S. Wang, H. Liu, Z. Wu, S. Yu, J. Holoubek, H. Zhou and P. Liu, Graphite-Based Lithium-Free 3D Hybrid Anodes for High Energy Density All-Solid- State Batteries, *ACS Energy Lett.*, 2021, **6**, 1831.

43 J. Duan, W. Wu, A. M. Nolan, T. Wang, J. Wen, C. Hu, Y. Mo, W. Luo and Y. Huang, Lithium-Graphite Paste: An Interface Compatible Anode for Solid-State Batteries, *Adv. Mater.*, 2019, **31**, 1807243.

44 C. Niu, H. Pan, W. Xu, J. Xiao, J.-G. G. Zhang, L. Luo, C. Wang, D. Mei, J. Meng, X. Wang, Z. Liu, L. Mai and J. Liu, Self-smoothing anode for achieving high-energy lithium metal batteries under realistic conditions, *Nat. Nanotechnol.*, 2019, **14**, 594.

45 F. Mo, J. Ruan, S. Sun, Z. Lian, S. Yang, X. Yue, Y. Song, Y. N. Zhou, F. Fang, G. Sun, S. Peng and D. Sun, Inside or Outside: Origin of Lithium Dendrite Formation of All Solid-State Electrolytes, *Adv. Energy Mater.*, 2019, **9**, 1902123.

46 W. Liu, Y. Xia, W. Wang, Y. Wang, J. Jin, Y. Chen, E. Paek and D. Mitlin, Pristine or Highly Defective?

Understanding the Role of Graphene Structure for Stable Lithium Metal Plating, *Adv. Energy Mater.*, 2019, **9**, 1802918.

47 Y. Gu, Y. He, L. Wei, Y. Lian, W. Pan, X. Li, Y. Su, Y. Peng, Z. Deng and Z. Liu, Fast-charging and dendrite-free lithium metal anode enabled by partial lithiation of graphene aerogel, *Nano Res.*, 2022, **15**, 9792.

48 X. Yu, S. Chen, B. Tang, X. L. Li, J. Zhou, Y. Ren, J. Wei, C. Yang, Y. Guo, Z. Zhou and S. H. Bo, The Debate over Hard Carbon and Alloy Anodes Continues for Solid-State Sodium Batteries, *ACS Energy Lett.*, 2024, **9**, 4441.

49 E. Olsson, G. Chai, M. Dove and Q. Cai, Adsorption and migration of alkali metals (Li, Na, and K) on pristine and defective graphene surfaces, *Nanoscale*, 2019, **11**, 5274.

50 O. Olaniyan, R. E. Maphasha, M. J. Madito, A. A. Khaleed, E. Igumbor and N. Manyala, A systematic study of the stability, electronic and optical properties of beryllium and nitrogen co-doped graphene, *Carbon*, 2018, **129**, 207.

51 H. Liang, J. Ni and L. Li, Bio-inspired engineering of Bi2S3-PPy yolk-shell composite for highly durable lithium and sodium storage, *Nano Energy*, 2017, **33**, 213.

52 Q. Meng, B. Deng, H. Zhang, B. Wang, W. Zhang, Y. Wen, H. Ming, X. Zhu, Y. Guan, Y. Xiang, M. Li, G. Cao, Y. Yang, H. Peng, H. Zhang and Y. Huang, Heterogeneous nucleation and growth of electrodeposited lithium metal on the basal plane of single-layer graphene, *Energy Storage Mater.*, 2019, **16**, 419.

53 S. K. Saju, S. Chattopadhyay, J. Xu, S. Alhashim, A. Pramanik and P. M. Ajayan, Hard carbon anode for lithium-, sodium-, and potassium-ion batteries: Advancement and future perspective, *Cell Rep. Phys. Sci.*, 2024, **5**, 101851.

54 X. Fan, W. T. Zheng, J.-L. L. Kuo and D. J. Singh, Adsorption of single Li and the formation of small Li clusters on graphene for the anode of lithium-ion batteries, *ACS Appl. Mater. Interfaces*, 2013, **5**, 7793.

55 H. Lv, Y. Yao, M. Yuan, G. Chen, Y. Wang, L. Rao, S. Li, U. I. Kara, R. L. Dupont, C. Zhang, B. Chen, B. Liu, X. Zhou, R. Wu, S. Adera, R. Che, X. Zhang and X. Wang, Functional nanoporous graphene superlattice, *Nat. Commun.*, 2024, **15**(1), 1295.

56 T. Hussain, E. Olsson, K. Alhameedi, Q. Cai and A. Karton, Functionalized Two-Dimensional Nanoporous Graphene as Efficient Global Anode Materials for Li-, Na-, K-, Mg-, and Ca-Ion Batteries, *J. Phys. Chem. C*, 2020, **124**, 9734.

57 P. C. Tsai, S. C. Chung, S. K. Lin and A. Yamada, Ab initio study of sodium intercalation into disordered carbon, *J. Mater. Chem. A*, 2015, **3**, 9763.

58 E. Olsson, J. Cottom and Q. Cai, Defects in Hard Carbon: Where Are They Located and How Does the Location Affect Alkaline Metal Storage?, *Small*, 2021, **17**, 2007652.

59 E. Olsson, J. Cottom, H. Au, M.-M. Titirici and Q. Cai, Investigating the effect of edge and basal plane surface functionalisation of carbonaceous anodes for alkali metal (Li/Na/K) ion batteries, *Carbon*, 2021, **177**, 226.

60 Z. Jian, C. Bommier, L. Luo, Z. Li, W. Wang, C. Wang, P. A. Greaney and X. Ji, Insights on the Mechanism of Na-Ion Storage in Soft Carbon Anode, *Chem. Mater.*, 2017, **29**, 2314.

61 L.-F. Zhao, Z. Hu, W.-H. Lai, Y. Tao, J. Peng, Z.-C. Miao, Y.-X. Wang, S.-L. Chou, H.-K. Liu, S.-X. Dou, L.-F. Z. Zhao, C. Miao, L.-F. Zhao, Z. Hu, W.-H. Lai, Y. Tao, J. Peng, Y.-X. Wang, S.-L. H. Chou, K. Liu and S.-X. Dou, Hard Carbon Anodes: Fundamental Understanding and Commercial Perspectives for Na-Ion Batteries beyond Li-Ion and K-Ion Counterparts, *Adv. Energy Mater.*, 2021, **11**, 2002704.

62 M. Liu, A. Kutana, Y. Liu and B. I. Yakobson, First-principles studies of Li nucleation on graphene, *J. Phys. Chem. Lett.*, 2014, **5**, 1225.

63 E. Lee and K. A. Persson, Li absorption and intercalation in single layer graphene and few layer graphene by first principles, *Nano Lett.*, 2012, **12**, 4624.

64 J. Vandevondele, M. Krack, F. Mohamed, M. Parrinello, T. Chassaing and J. Hutter, Quickstep: Fast and accurate density functional calculations using a mixed Gaussian and plane waves approach, *Comput. Phys. Commun.*, 2005, **167**, 103.

65 J. VandeVondele and J. Hutter, Gaussian basis sets for accurate calculations on molecular systems in gas and condensed phases, *J. Chem. Phys.*, 2007, **127**, 114105.

66 J. Hutter, M. Iannuzzi, F. Schiffmann and J. Vandevondele, Cp2k: Atomistic simulations of condensed matter systems, *Wiley Interdiscip. Rev.: Comput. Mol. Sci.*, 2014, **4**, 15.

67 K. Burke, F. G. Cruz and K.-C. Lam, Unambiguous exchange-correlation energy density, *J. Chem. Phys.*, 1998, **109**, 8161.

68 T. D. Kühne, M. Iannuzzi, M. Del Ben, V. V. Rybkin, P. Seewald, F. Stein, T. Laino, R. Z. Khaliullin, O. Schütt, F. Schiffmann, D. Golze, J. Wilhelm, S. Chulkov, M. H. Bani-Hashemian, V. Weber, U. Borštnik, M. Taillefumier, A. S. Jakobovits, A. Lazzaro, H. Pabst, T. Müller, R. Schade, M. Guidon, S. Andermatt, N. Holmberg, G. K. Schenter, A. Hehn, A. Bussy, F. Belleflamme, G. Tabacchi, A. Glöß, M. Lass, I. Bethune, C. J. Mundy, C. Plessl, M. Watkins, J. VandeVondele, M. Krack and J. Hutter, CP2K: An electronic structure and molecular dynamics software package - Quickstep: Efficient and accurate electronic structure calculations, *J. Chem. Phys.*, 2020, **152**, 194103.

69 M. Krack, Pseudopotentials for H to Kr optimized for gradient-corrected exchange-correlation functionals, *Theor. Chem. Acc.*, 2005, **114**, 145.

70 S. Goedecker, M. Teter and J. Hutter, Separable dual-space Gaussian pseudopotentials, *Phys. Rev. B:Condens. Matter Mater. Phys.*, 1996, **54**, 1703.

71 C. Hartwigsen, S. Goedecker and J. Hutter, Relativistic separable dual-space Gaussian pseudopotentials from H to Rn, *Phys. Rev. B:Condens. Matter Mater. Phys.*, 1998, **58**, 3641.

72 C. G. Broyden, The convergence of a class of double-rank minimization algorithms 1. General considerations, *IMA J. Appl. Math.*, 1970, **6**, 76.

73 D. Goldfarb, A Family of Variable-Metric Methods Derived by Variational Means, *Math. Comput.*, 1970, **24**, 23.

74 D. F. Shanno, Conditioning of Quasi-Newton Methods for Function Minimization, *Math. Comput.*, 1970, **24**, 647.

75 R. Fletcher, A new approach to variable metric algorithms, *Comput. J.*, 1970, **13**, 317.

76 J. D. Head and M. C. Zerner, A Broyden-Fletcher-Goldfarb-Shanno optimization procedure for molecular geometries, *Chem. Phys. Lett.*, 1985, **122**, 264.

77 J. Perdew, K. Burke and M. Ernzerhof, Errata: Generalized Gradient Approximation Made Simple, *Phys. Rev. Lett.*, 1997, **77**, 3865.

78 J. Perdew, K. Burke and M. Ernzerhof, Generalized Gradient Approximation Made Simple, *Phys. Rev. Lett.*, 1997, **78**, 1396.

79 A. D. Becke and E. R. Johnson, Density-functional thermochemistry. III. The role of exact exchange, *J. Chem. Phys.*, 2005, **123**, 154108.

80 E. R. Johnson and A. D. Becke, A post-Hartree-Fock model of intermolecular interactions: Inclusion of higher-order corrections, *J. Chem. Phys.*, 2006, **124**, 174104.

81 S. Grimme, S. Ehrlich and L. Goerigk, Effect of the Damping Function in Dispersion Corrected Density Functional Theory, *J. Comput. Chem.*, 2011, **32**, 1456.

82 S. Grimme, J. Antony, S. Ehrlich and H. Krieg, A consistent and accurate ab initio parametrization of density functional dispersion correction (DFT-D) for the 94 elements H-Pu, *J. Chem. Phys.*, 2010, **132**, 154104.

83 S. Grimme, J. Antony, T. Schwabe and C. Mück-Lichtenfeld, Density functional theory with dispersion corrections for supramolecular structures, aggregates, and complexes of (bio)organic molecules, *Org. Biomol. Chem.*, 2007, **5**, 741.

84 E. Olsson, J. Cottom, H. Alptekin, H. Au, M. Crespo-Ribadeneyra, M. M. Titirici and Q. Cai, Investigating the Role of Surface Roughness and Defects on EC Breakdown, as a Precursor to SEI Formation in Hard Carbon Sodium-Ion Battery Anodes, *Small*, 2022, **18**, 2200177.

85 J. Jiao, R. Xiao, M. Han, Z. Wang and L. Chen, Impact of Hydrogen on Lithium Storage on Graphene Edges, *Appl. Surf. Sci.*, 2020, 145886.

86 J. Cottom, S. van Vliet, J. Meyer, R. Bliem and E. Olsson, Coverage-dependent stability of Ru x Si y on Ru(0001): a comparative DFT and XPS study, *Phys. Chem. Chem. Phys.*, 2024, **26**, 28793.

87 S. Zhang and J. Northrup, Chemical potential dependence of defect formation energies in GaAs: Application to Ga self-diffusion, *Phys. Rev. Lett.*, 1991, **67**, 2339.

88 J. Gaberle, D. Z. Gao, M. B. Watkins and A. L. Shluger, Calculating the Entropy Loss on Adsorption of Organic Molecules at Insulating Surfaces, *J. Phys. Chem. C*, 2016, **120**, 3913.

89 C. Sutton and S. V. Levchenko, First-Principles Atomistic Thermodynamics and Configurational Entropy, *Front. Chem.*, 2020, **8**, 757.

90 F. Friedrich, S. Pieper and H. A. Gasteiger, Entropy Measurements of Li-Ion Battery Cells with Li- and Mn-Rich Layered Transition Metal Oxides via Linear Temperature Variation, *J. Electrochem. Soc.*, 2021, **168**, 120502.

91 K. Momma and F. Izumi, VESTA 3 for three-dimensional visualization of crystal, volumetric and morphology data, *J. Appl. Crystallogr.*, 2011, **44**, 1272–1276.

92 R. S. Mulliken and J. Chem Phys, Electronic Population Analysis on LCAO-MO Molecular Wave Functions. I, *J. Chem. Phys.*, 1955, **23**, 1833.

93 K. Nakada and A. Ishii, DFT Calculation for Adatom Adsorption on Graphene, in *Graphene Simulation*, ed. J. Gong, InTech, 2011, ch. 1, pp. 3–19.

94 S. Yang, S. Li, S. Tang, W. Dong, W. Sun, D. Shen and M. Wang, Sodium adsorption and intercalation in bilayer graphene from density functional theory calculations, *Theor. Chem. Acc.*, 2016, **135**, 1.

95 D. Shpalter, Z. V. Bobyleva, G. P. Lakienko, A. R. Safiullina, A. Jablanovic, D. S. Lutsenko, O. A. Drozhzhin and E. V. Antipov, Hard carbon anode materials for hybrid sodium-ion/metal batteries with high energy density, *J. Power Sources*, 2024, **624**, 235547.

96 F. Xie, Z. Xu, Z. Guo and M.-M. Titirici, Hard carbons for sodium-ion batteries and beyond, *Prog. Energy*, 2020, **2**(4), 042002.

97 Z. Jian, Z. Xing, C. Bommier, Z. Li and X. Ji, Hard Carbon Microspheres: Potassium-Ion Anode Versus Sodium-Ion Anode, *Adv. Energy Mater.*, 2016, **6**, 1501874.

98 D. Chen, W. Zhang, K. Luo, Y. Song, Y. Zhong, Y. Liu, G. Wang, B. Zhong, Z. Wu and X. Guo, Hard carbon for sodium storage: Mechanism and optimization strategies toward commercialization, *Energy Environ. Sci.*, 2021, **14**, 2244.

99 J. Zhao, X. Zou, Y. Zhu, Y. Xu and C. Wang, Electrochemical Intercalation of Potassium into Graphite, *Adv. Funct. Mater.*, 2016, **26**, 8103.

100 Z. Chen, L. Wang, J. Zheng, Y. Huang, H. Huang, C. Li, Y. Shao, X. Wu, X. Rui, X. Tao, H. Yang and Y. Yu, Unraveling the Nucleation and Growth Mechanism of Potassium Metal on 3D Skeletons for Dendrite-Free Potassium Metal Batteries, *ACS Nano*, 2024, **18**, 8496.